Shape evolution of a melting nonspherical particle

Daniel M. Kintea,[1] Tobias Hauk,[2] Ilia V. Roisman,[1,*] and Cameron Tropea[1]

[1]*Institute for Fluid Mechanics and Aerodynamics, Center of Smart Interfaces, Technische Universtität Darmstadt, D-64287 Darmstadt, Germany*

[2]*Airbus Group Innovations, Munich D-81663, Germany*

(Received 14 May 2015; revised manuscript received 12 June 2015; published 14 September 2015)

In this study melting of irregular ice crystals was observed in an acoustic levitator. The evolution of the particle shape is captured using a high-speed video system. Several typical phenomena have been discovered: change of the particle shape, appearance of a capillary flow of the melted liquid on the particle surface leading to liquid collection at the particle midsection (where the interface curvature is smallest), and appearance of sharp cusps at the particle tips. No such phenomena can be observed during melting of spherical particles. An approximate theoretical model is developed which accounts for the main physical phenomena associated with melting of an irregular particle. The agreement between the theoretical predictions for the melting time, for the evolution of the particle shape, and the corresponding experimental data is rather good.

DOI: 10.1103/PhysRevE.92.033012 PACS number(s): 47.55.Kf, 64.70.dj, 47.55.nb

I. INTRODUCTION

Phase change processes on spherical solids have always been of fundamental interest. Typical examples include the well-known Stefan and Neumann problems [1]. One of the simplest cases of a Stefan problem is melting of a solid sphere. Such one-dimensional problem includes a solution for the heat conduction in the solid and liquid regions of the sphere and matching using the Stefan condition at the solid-liquid boundary. For a sphere heated by an external gas flow also the thermal boundary conditions on the liquid surface have to be considered, which account for the convection in the outer gas region. Despite its "simplicity" this problem still does not have an exact analytical solution. The problem becomes especially complicated if the initial temperature of the solid particle is not uniform or even if it is not equal to the fusion temperature.

Among theoretical models, the problem of phase change of a sphere at various asymptotic conditions are models developed for small Stefan numbers [2–7], short time asymptotic solutions [7–9], and remote asymptotic solutions for long times [6,10]. Results valid for general Stefan numbers are obtained numerically [7] and analytically [11].

Simplified models allowing one to roughly estimate the typical melting times and rates of melting are also very useful for various engineering applications, mainly if the heat conduction in the solid particle and thermal transient effects are negligibly small [12,13]. A simplified one-dimensional model has been proposed by Mason [14]. Such a model, which assumes the melting particle to be spherical and isothermal, is widely used [15–17]; also in applications involving the melting of nonspherical particles [18–20].

A description of a phase change, melting or condensation, at a surface of solid bodies of irregular shape is even a more challenging problem. This problem is associated with melting of clusters of particles [21], melting or condensation in porous media [22,23], in suspensions [24] or in granular media [25–27], and melting of snow flakes [28,29] or other dendritic structures [30]. Melting of solid particles is a key element in thermal spraying technology [31,32] or in the production of spherical particles. This problem is also associated with phase-change materials for energy storage components [33].

Melting of particles in the submicron size range have also attracted much interest, including studies on the dependence of the melting temperature on the particle size [34–36], or even on the size dispersity [37]. Melting of particles, in particular irregular particles [38], is an important element of the technology of selective laser sintering, which is a rapid prototyping technique for fabrication of components with complex geometries and from complex materials; for example, sintered metallic parts [39] or artificial bones [40].

Atmospheric ice crystals can adhere and accrete at the internal surfaces of jet engines or aircraft instrumentation [41] if they partially melt. Ice accretion reduces the engine's reliability, power, and efficiency. Atmospheric ice crystals usually form due to condensation and desublimation, leading to various geometries such as needles, plates, prisms, or dendrites [42,43]. The melting behavior of such particles differs significantly from spherical ones.

Some experimental studies on particle melting have been undertaken in the past; for example, investigations of snow flakes [28,29] or other dendritic structures [30]. Wind tunnel experiments are often used to investigate the melting of ice spheres [44–46] under conditions similar to real flight conditions.

For many applications in which particle melting is involved, a knowledge about the temporal evolution of the liquid part is necessary for a better prediction of associated physical phenomena. A one-dimensional model, based on a spherical geometry of the particle cannot provide accurate data for the volume of the liquid portion of the particle since it does not capture the flow along the particle surface.

This study presents an experimental investigation and a theoretical model for the melting process of an irregular, nonspherical particle. The model accounts for the main phenomena associated with irregular particles and observed in experiments, namely, the capillary flow of the melted liquid, leading to its collection at the particle midsection, where the interface curvature is smallest, and appearance of the cusps at the particle tips. The results obtained with this

*roisman@sla.tu-darmstadt.de

model are compared with experimental data of melting of grinded irregular ice particles. It is shown that the composition of the ice particles deviates significantly throughout the melting process from that of spherical particles, resulting in a significant impact on the icing behavior. The theoretical predictions agree well with the experimental data.

II. EXPERIMENTAL METHOD

An experimental study for melting of irregular ice particles was carried out to observe the variation of their shapes and to measure the typical times, corresponding to the complete transformation into a spherical drop and to complete particle melting. In these experiments ice particles in an acoustic levitator [47,48] are melted by a forced convection flow with variation of particle size and shape, temperature, and humidity of the incident air flow as well as the flow velocity.

A. Experimental setup

In Fig. 1 a sketch of the experimental setup is shown. The main components of the setup are an acoustic levitator used to suspend single ice particles, an optical and recording system to record the melting particle with a decent magnification, and a flow supply and control system which generates a defined air flow.

a. Acoustic levitator. An acoustic levitator (tec5 AG, Oberursel, Germany) is used for suspension of a particle in a standing acoustic wave, generated between an ultrasound transducer and concave reflector. The working frequency of the levitator is 58 kHz.

Several equally spaced nodes and antinodes of sound particle velocity and sound pressure can be identified in the standing wave. Particles, whose density ranges from 0.5 to 2 g/cm^3, can be levitated just below the pressure nodes in the stable region due to the axial levitation force and the Bernoulli stress which stabilizes the suspended particle radially. The magnitude of the acoustic force is controlled by setting the power level of the acoustic levitator.

In our experiments the acoustic levitator is located in a chest freezer. This allows one to keep a definite initial ice particle temperature determined by the surrounding temperature. The surrounding, hence the initial ice particle temperature, is measured by a resistive temperature detector (RTD) sensor (Pt100) attached to the levitator close to the ice particle position. A DP9602 high accuracy digital thermometer (OMEGA, Stamford, USA) is used.

b. Flow supply and control system. The ice particle is melted by a warm, uniform, and controlled airflow. The pressurized air (at 1 bar and 20 °C) is passed through several gas washing bottles filled with water to control the relative humidity of the airflow. The humidified air is then passed through a coil of copper tube immersed in a temperature-controlled water bath to control the air temperature. The mass flow rate of the pressurized air is controlled using an FMA-2600 mass flow controller (OMEGA, Stamford, USA).

Finally, the air flows through a flow tube which contains 20 screens to generate a nearly uniform velocity profile in the experimental cell. The tube, made of aluminum, is thermally insulated.

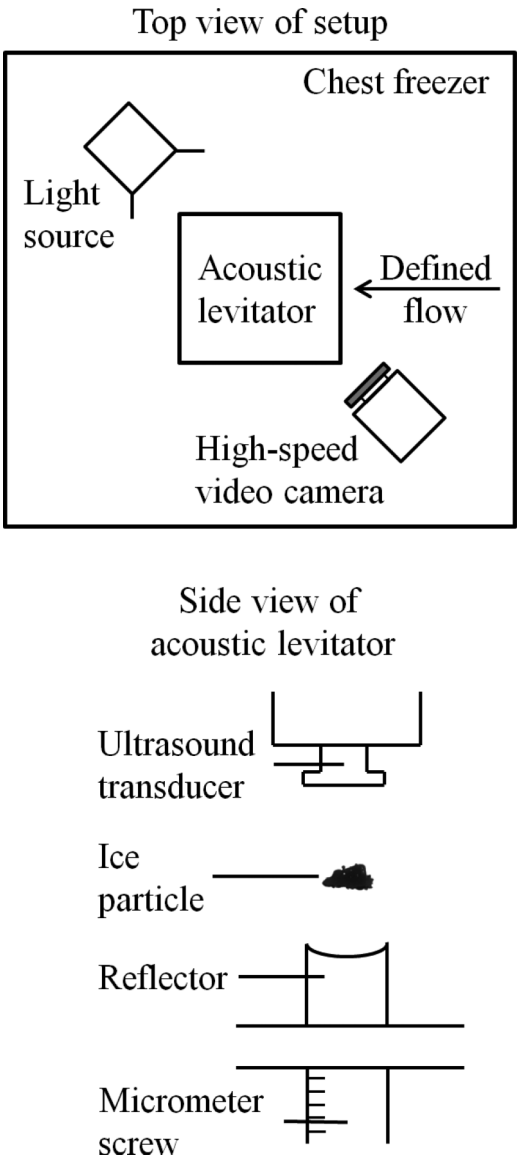

FIG. 1. Sketch of the experimental setup and levitator.

The levitated ice particle is positioned on the extended axis of the flow tube and is located approximately 5 mm away from the tube open end.

The temperature of the airflow is measured with a RTD sensor (Pt100). A B-530 humidity sensor connected to a GL220 data logger (both from Graphtec Corporation, Yokohama, Japan) is used to measure the relative humidity. A pressure transducer system (Aerolab LLC, Laurel, USA) measures the ambient pressure.

c. Optical and recording system. A Phantom v611 high-speed video camera (Vision Research Inc., Wayne, USA) attached to a SZX10 microscope (Olympus Corporation, Tokyo, Japan) is used for the observation of the melting process. A Dedocool cold light source (Dedo Weigert Film GmbH, Munich, Germany) illuminates the ice particle suspended in the acoustic field. Frame rates of the camera during capturing of the melting process ranged from 120 to 250 fps. Typical values of pixel resolution, exposure time, and overall resolution were

approximately 156 pixels per mm, 500 μs, and 752 × 504 pixels, respectively.

Between flow and line of sight, there is an angle of approximately 50°. That means that the true dimensions of the ice particle during its melting have to be corrected accounting for the particle orientation in the levitator. The majority of the particles is usually aligned perpendicular to the flow. Therefore, the estimation of the particle dimensions from its projection on the camera view can be based on the known angle between the flow vector and the axis of view. This angle (50°) is determined by the configuration of the levitator.

B. Test procedure and conditions

a. Particle generation. Nonspherical ice particles are collected from the ice layer grown on the walls of a chest freezer at temperatures in the range of −15 to −25 °C. Cold tweezers are then used to place an ice particle in the acoustic levitator.

A spherical ice particle is generated by melting a nonspherical ice particle until approximately 90% of its mass is liquid. Then, the warm airflow is stopped and a spherical particle is generated by refreezing, usually within seconds due to the residual ice core acting as a seed for crystallization.

*b. Particle melting.*The power of the acoustic levitator is adjusted to ensure that the particle will not be blown out of the acoustic field by the airflow but the shape of the completely melted ice particle will not be strongly distorted by an acoustic pressure and remains nearly spherical. By adjusting the mass flow controller and the temperature of the water bath, the flow velocity and temperature are set.

When steady-state airflow conditions are reached, the flow tube, which is initially kept outside of the chest freezer, is placed in its mount next to the ice particle. A few seconds before the placement of the tube in its mount, the camera is started to record both the initial unaffected particle and the melting process.

Exemplary time sequences captured using the camera are shown in Figs. 2–4. Due to the melting of the irregular particle not only the size of the solid part reduces, but also its irregularities are smoothed. The melted liquid is always collected in the midsection of the particle. After some time sharp cusps are formed at the particle tips. Such phenomena do not occur during melting of a spherical particle (Fig. 4) due to symmetry of its geometry. Similar phenomena have been observed during ice flakes melting [50].

The ice particle shown in Fig. 3 breaks up during melting. Such a possibility has been previously mentioned for snow flakes [50,51].

III. APPROXIMATE MODEL FOR THE PARTICLE SHAPE

A. Mechanisms of particle melting

Five main stages of the melting process can be identified. Stage I is characterized by the warming of a particle without phase change up to the melting temperature. In stage II the particle begins to melt, leading to water accumulation in the area of lowest curvature, as can be seen in Figs. 2 and 3. The shape of the liquid water is determined by the total volume of the melted liquid and by the contact angle,

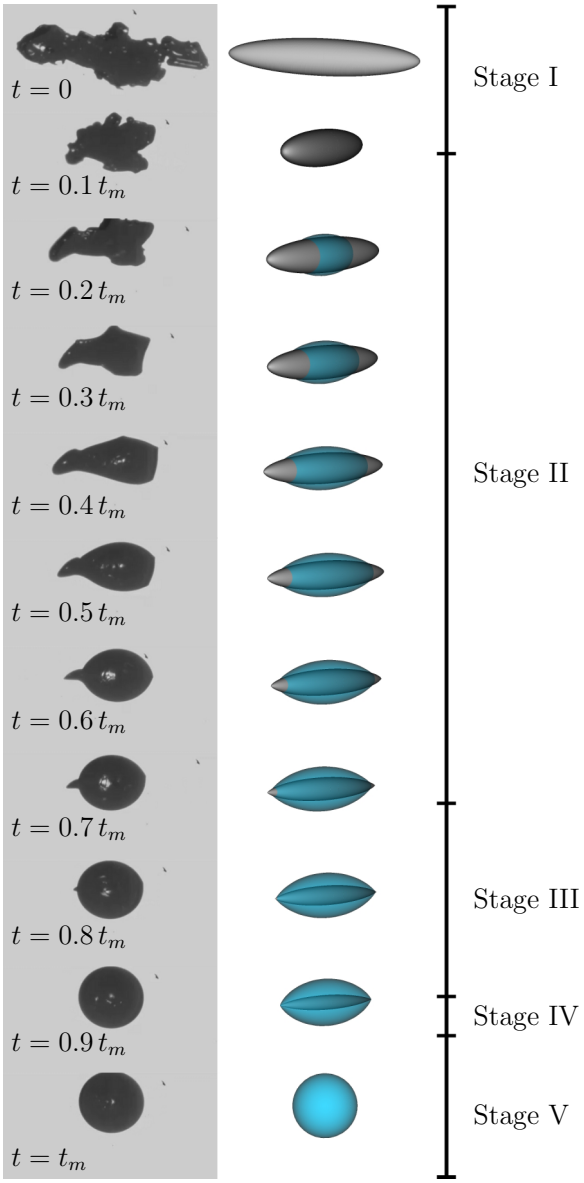

FIG. 2. (Color online) Comparison of the noncollapsing ice particle shape with the theoretical predictions for the operational conditions corresponding to case 1 from Table I. Experimental results are shown on the left, while the corresponding computed shape is shown on the right. The observed movie of particle melting is available online [49].

which for ice is $\Theta = 12^\circ$ [52]. The apparently dry portions of the particle surface are in fact wetted due to melting. The thickness of the liquid film in these regions is small; however, the camera does not resolve this film. During stage III the solid particle is completely covered by a nonspherical liquid droplet, pinned at the particle tips. In stage IV the length of the ice portion is smaller than the drop diameter—the particle is completely immersed in the liquid drop. In the final stage V the completely melted liquid drop is heated above the melting temperature.

During the first stage (I) the thermal effects associated with the temperature gradients in the solid, and development of the thermal boundary layer, are small. The lumped capacitance method predicts the evolution of the average particle

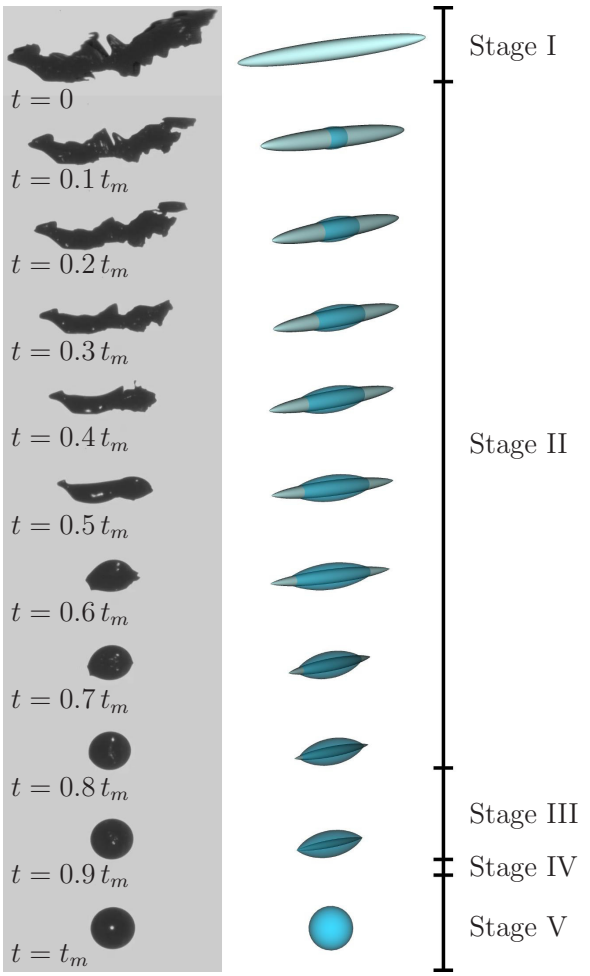

FIG. 3. (Color online) Comparison of the observed particle shape with the theoretical predictions for the operational conditions corresponding to case 2 from Table I. At $t \approx 0.55t_m$ the particle collapses due to surface tension of the accumulated melted water. The corresponding movies are available online [49].

temperature rather well since the Biot number of the particle, $\mathrm{Bi} = \mathrm{Nu}k_a/k_p$, is small. Here Nu is the Nusselt number, and k_a and k_p are the thermal conductivities of the air and of the particle, respectively.

During the second stage (II) the mechanism of melting of a nonspherical particle is influenced significantly by a capillary flow of the melted liquid on the particle surface. The pressure in a liquid film covering the particle of a typical size a can be estimated using the Young-Laplace equation, $p \sim \gamma/a$, where γ is the surface tension of the liquid. The typical velocity in the film of thickness h_f is estimated from the mass balance equation as $u \sim u_m a/h_f$, where u_m is the typical melting velocity. This velocity can be estimated from experiments through $u_m \sim a/t_m$. Here t_m is the total melting time. Finally, the film thickness can be estimated from the momentum balance equation $p/a \sim \eta u/h_f^2$ (η being the liquid viscosity) which considers the forces related to the pressure gradient in the liquid film and the viscosity effects. The resulting estimation for the liquid film thickness is

$$h_f \sim \frac{a^{4/3}\eta^{1/3}}{\gamma^{1/3}t_m^{1/3}}. \quad (1)$$

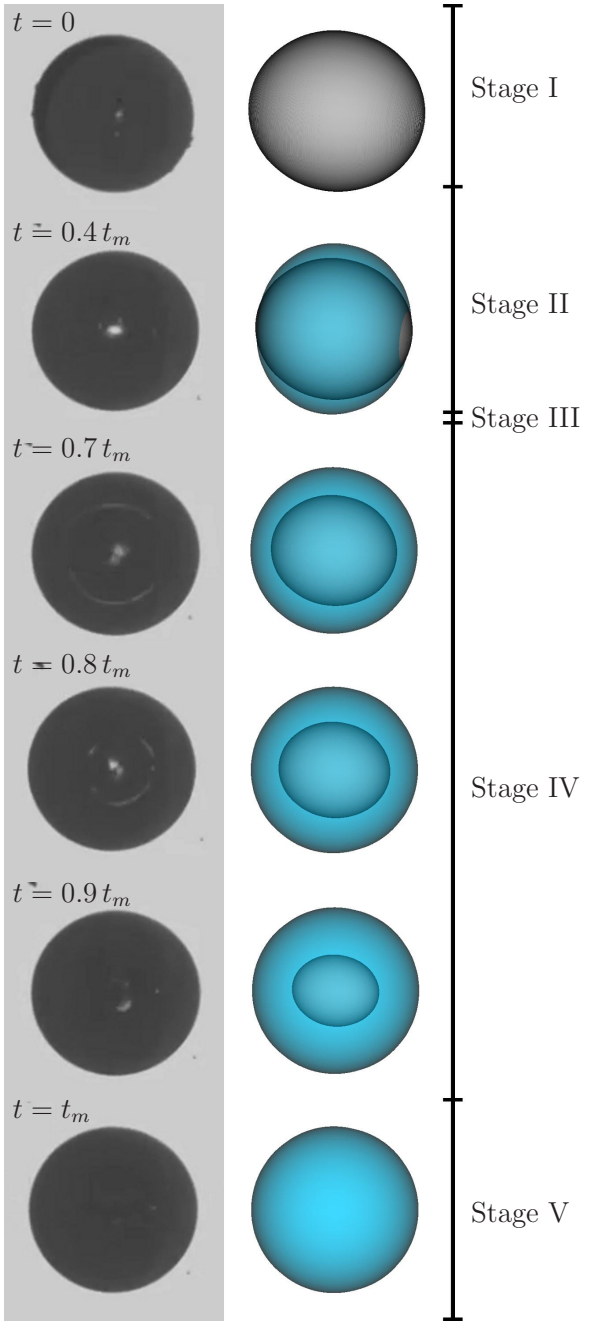

FIG. 4. (Color online) Comparison of a nearly spherical ice particle shape with the theoretical predictions for the operational conditions corresponding to case 3 from Table I, and aspect ratio of $E = 1.1$. As a result of the low aspect ratio, the melting stages II and III make up only a small fraction of the entire melting time. Most of the melting takes place in stage IV, which corresponds to the 1D sphere model. The observed movie of particle melting is available online [49].

In our experiments the typical melting time of a millimetric particle is approximately 10^1 seconds. Expression (1) yields $h_f \sim 10$ μm. The influence of the thin film on the heat transfer in the particle is rather small. It will be neglected in the further analysis.

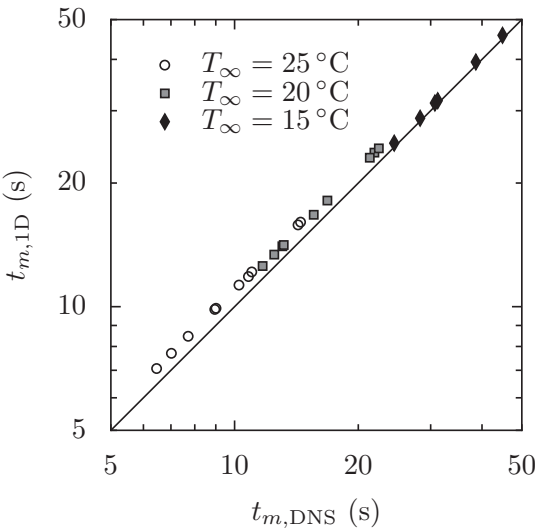

FIG. 5. Comparison between melting times obtained by the isothermal sphere model and from a detailed numerical simulation (DNS), taking into account the temperature field in the spherically assumed ice particle. Results were generated assuming an ambient pressure of $p_\infty = 96$ kPa, a flow velocity of 1 m/s, dry air, and an initial particle temperature of 255 K. The size of the particles varies between 0.5 and 0.8 mm.

B. Main assumption for modeling

Since the thermal conductivity of the particle is much higher than that of the surrounding gas, the temperature gradient in the particle is relatively small. The Stefan number

$$\mathrm{St} \equiv \frac{c_p \Delta T}{L}, \tag{2}$$

represents the ratio of the sensible heat to the heat spent on melting. In our case the specific heat for ice is $c_{p,\mathrm{ice}} = 2060$ and for water is $c_{p,\mathrm{water}} = 4180\,\mathrm{J/(kg\,K)}$, and the latent heat of melting $L = 3.33 \times 10^5\,\mathrm{J/kg}$. The maximum Stefan numbers in our experiments are therefore $\mathrm{St}_{\mathrm{ice}} \approx 0.12$ for ice and $\mathrm{St}_{\mathrm{ice}} \approx 0.3$ for water. These numbers are based on $\Delta T = T_m - T_0 = 20\,^\circ\mathrm{C}$ for ice and $\Delta T = T_\infty - T_m = 25\,^\circ\mathrm{C}$ for water, where T_m is the melting temperature, T_0 is the initial particle temperature, and T_∞ is the surrounding gas temperature.

Since the Stefan numbers are small, the particle can be considered to be isothermal throughout the melting process as has already been assumed by Mason [14] for spherical geometry. Figure 5 compares melting times of spherical particles once obtained by the one-dimensional isothermal sphere model $t_{m,1\mathrm{D}}$ and once by a detailed numerical simulation which takes into account heat conduction in solid and liquid regions of the melting spherical particle $t_{m,\mathrm{DNS}}$. The employed numerical algorithm is based on the enthalpy method and is spatially discretized one dimensionally using finite volumes. In this approach no liquid flow is considered and therefore only conductive heat fluxes are accounted for in the solid and the liquid phase. A heat flux, derived from suitable Nusselt correlations, is applied on the outer boundary of the initially solid particle. This heat flux heats the particle up nonuniformly until it reaches its fusion temperature, followed by the movement of the solid-liquid interface towards the particle center.

It is known that modeling of the melting of nanoparticles leads to the appearance of a singularity in the solution as the particle radius goes to zero. At small particle radii the effect of the dependence of the melting temperature on the particle curvature becomes significant. Back *et al.* [53] show that this singularity can be avoided by accounting for the kinetic effects. The total melting time of a nanoparticle is finite and much shorter than the typical melting time considered in our experiments. Therefore, the singularity effects almost do not affect the results of the present study.

The deviation between the two models slightly increases as the flow temperature, and therefore the heat flux, rises. Also, a dependency on the particle size is observed. This dependency has nearly no influence when considering ice particles of the size of a few millimeters suspended in air. In all considered cases, the isothermal sphere model yields slightly lower melting times than the detailed numerical simulation. This is explained by the time the heat needs to be conducted towards the ice core of the particle, which is neglected in the isothermal model. Anyhow, the deviations are rather low when considering ice particles suspended in air and moderate temperature differences. The assumption of isothermal particle will then be applied also to the description of nonspherical particle.

C. Numerical algorithm

It is known that heat transfer coefficients depend on the particle shape, and that the heat flux at the particle surface is not uniform. Nevertheless, these effects are secondary in comparison with the influence of the liquid redistribution. Therefore, as a zero approximation we assume a uniform distribution of the average heat flux on the particle surface, which is derived from the heat transfer for a volume-equivalent sphere. In this case the evolution of the particle shape is determined completely by the uniform melting velocity u_m and is described by an eikonal equation [54]. In fact, the problem is reduced to the computation of the surface propagation with a uniform velocity in the normal direction. For a three-dimensional case the most convenient technique of solution of this equation is based on the level-set method [55]. This computational method allows calculation of equidistant surfaces which describe the shape of the melting particle in time assuming a uniformly distributed heat flux. The family of these surfaces is determined only by the initial body shape.

In Fig. 6 two examples of the surface evolutions are shown, which are analogous to a melting of a single bump on a planar surface, and to the melting of a spheroid. These simulations explain the smoothing of a surface leading to the bump elimination. Similar surface smoothing has been observed earlier during melting of artificial hailstones [56]. The example in Fig. 6 demonstrates also an appearance of the sharp cusps, where the local curvature radius vanishes. This situation is analogous to the mechanism of cusp formation on a rim bounding a free liquid sheet [57,58] and analyzed in the study on the emergence of singularities during melting processes [59]. The cusp is formed since the local curvature radius changes linearly with the propagation distance of the

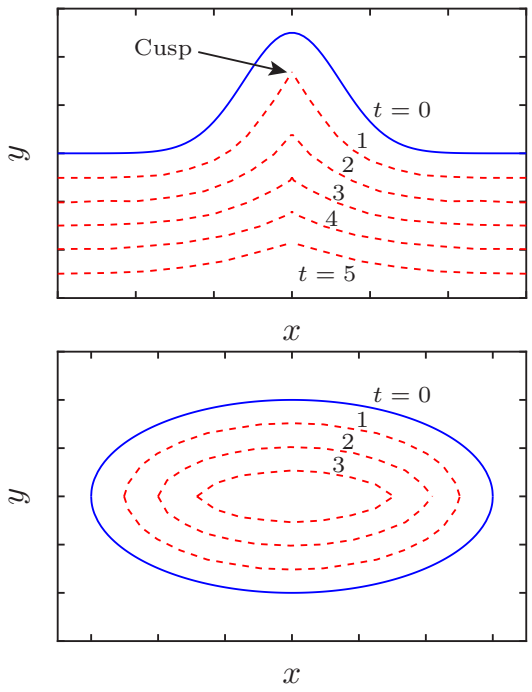

FIG. 6. (Color online) Examples of the theoretically predicted evolutions of the shapes of a bump on a planar surface, and of an ellipse. The dimensionless velocity $u_m = 1$.

interface. At some time instant the curvature vanishes, which corresponds to the appearance of the cusp.

Stages II and III do not appear during the melting of a spherical particle. The heat transfer and particle melting during phases IV and V can be well predicted by the well-known models based on the spherical drop or particle shape [1].

D. Estimation of the heat flux and of the typical melting rate

In order to describe the melting process of a nonspherical particle we approximate its initial shape by a spheroid, keeping the volume and the maximum dimension $D_{\max}$ the same as for the particle. The melting velocity u_m is evaluated from the energy balance. The heat flux at the particle surface [60] is determined by the particle and surrounding gas temperatures, particle relative velocity, and the thermodynamic properties of the gas.

Applying the heat and mass transfer coefficients of a volume equivalent sphere on the surface A_A of the solid and/or liquid particle which is in direct contact with the airflow yields the heat flux

$$\dot{Q} = A_A\left[\alpha(T_\infty - T_P) + \beta(C_\infty - C_P)L_{\text{ev}}M_{\text{H}_2\text{O}}\right]. \quad (3)$$

Heat and mass transfer coefficients are denoted by α and β, while T and C stand for temperature and mole fraction. The indices correspond to far-field conditions (∞) and values at the particle surface (P). This heat flux is composed of a convective heat transfer component visible in Eq. (3) as the first term in brackets. The second term is a specific mole flux multiplied with the latent heat of evaporation L_{ev} and the molar mass of water $M_{\text{H}_2\text{O}}$ yielding the heat transfer accompanying a convective mass flux, e.g., evaporative cooling. A suitable Nusselt correlation [60] for a sphere is employed to derive the heat and mass transfer coefficients. This Nusselt number Nu_{Sp} of a sphere comprises a laminar component

$$\text{Nu}_{\text{lam}} = 0.664\sqrt{\text{Re}}\,\text{Pr}^{1/3}, \quad (4)$$

and a turbulent contribution

$$\text{Nu}_{\text{turb}} = \frac{0.037\,\text{Re}^{0.8}\,\text{Pr}}{1 + 2.443\,\text{Re}^{-0.1}(\text{Pr}^{2/3} - 1)}, \quad (5)$$

where Re and Pr denote the Reynolds and Prandtl number, respectively. Blending the two components by

$$\text{Nu}_{\text{Sp}} = 2 + \sqrt{\text{Nu}_{\text{lam}}^2 + \text{Nu}_{\text{turb}}^2}, \quad (6)$$

yields the Nusselt number for a sphere. This value is used to derive the applicable heat transfer coefficient

$$\alpha = \frac{\text{Nu}_{\text{Sp}}\,k_a}{d_{\text{eq}}}, \quad (7)$$

where k_a is the thermal conductivity of the surrounding fluid and d_{eq} corresponds to the diameter of a volume equivalent sphere which is the characteristic length of the problem. The mass transfer coefficient is computed with the same set of equations by substituting Pr with the Schmidt number $\text{Sc} = \eta_a/(\rho_a D)$ and Nu with the Sherwood number $\text{Sh} = \beta\, d_{\text{eq}}/D$. The diffusion coefficient of the material the particle is made of in the ambient fluid is denoted by D while η_a denotes the surrounding fluid's dynamic viscosity. Assuming that the obtained heat flux $\dot{Q}$ is evenly spread over the surface of the solid ice A_I yields the melting velocity $\boldsymbol{u}_m$ which is constant over the surface. It reads

$$\boldsymbol{u}_m = -\frac{\dot{Q}}{L_m \rho A_I} \cdot \boldsymbol{n}, \quad (8)$$

where the vector $\boldsymbol{n}$ is the unit normal vector on the surface of the ice, L_m is the latent heat of fusion, and ρ is the density of the ice. By integrating this velocity over the time t a new shape of the solid fraction of the particle is found which is subsequently used to obtain the melted volume V_m.

IV. RESULTS AND DISCUSSION

In the second phase the shape of the solid part is computed using the level-set method, mentioned above. The volume of the liquid is estimated from the mass balance of the entire particle. Since the dynamic effects in the liquid portion are small, its quasistatic shape can be approximated by an axisymmetric constant-mean-curvature surface, whose analytical solution is known [61].

In the cylindrical coordinate system the shape of the liquid interface has to satisfy the following equation:

$$\frac{1 + R_z^2 - RR_{zz}}{R\left(1 + R_z^2\right)^{3/2}} = \kappa, \quad (9)$$

where R is the radius of the local interface, and z is the axial coordinate. The local curvature κ is constant.

The solution of (9) yields

$$z = \pm \int \frac{dR}{\sqrt{\frac{4R^2}{\kappa^2(R^2 - c)^2} - 1}}, \quad (10)$$

TABLE I. Operating conditions for the presented cases 1–3. Ambient pressure and temperature are denoted by p_∞ and T_∞, respectively, while T_0 corresponds to the initial particle temperature. The relative humidity of the flow is denoted by φ which flows at a velocity of u and the particle shape is characterized by its maximum dimension $D_{\max}$, initial mass m_0, and aspect ratio E. Measured overall melting times are denoted by $t_{m,\text{expt}}$.

		Case 1	Case 2	Case 3
p_∞	(kPa)	95.30	95.87	95.33
T_∞	(K)	288.25	292.88	293.22
T_0	(K)	254.75	257.53	255.95
φ	(%)	61	4	56
u	(m/s)	0.751	0.990	1.25
$D_{\max}$	(mm)	2.43	3.49	0.837
m_0	(ng)	267.4	232.2	233.6
$t_{m,\text{expt}}$	(s)	14.46	13.78	7.06
E	(−)	5.07	9.39	1.1

where c and κ are constants, obtained from the conditions of a given volume of the liquid part and a given local contact angle.

Examples of the theoretical predictions of the particle shape are shown in Figs. 2–4. The predictions agree rather well with the observed particle shapes. Operational parameters of these three cases are given in Table I. Case 1 is a typical case where irregularities are smoothed in the beginning of the melting process and sharp cusps appear at a later stage. Figure 7 shows the projected particle length l_{proj} nondimensionalized with the diameter of a volume-equivalent sphere d_{eq} over time. For the computation of the projected length the particle is assumed to align with an angle of 50° to the line of sight owing to the experimental setup.

The melting process of case 2 exhibits peculiarities which could be observed in approximately 10% of the cases. At $t \approx 0.55t_m$ the particle collapses due to surface tension forces in the accumulated meltwater. Such a particle collapse usually results in a less precise prediction of the melting time, as the surface area evolution deviates from the idealized one. This collapse also manifests itself in the evolution of the projected particle length. Figure 8 shows this length over time for case 2. After the collapse, the particle is nearly spherical in the experiment.

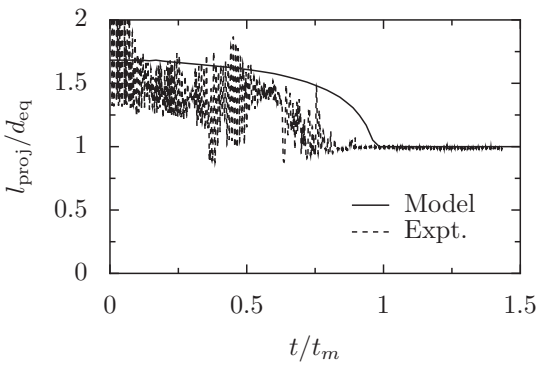

FIG. 7. Projected length l_{proj}, nondimensionalized with the diameter of a volume-equivalent sphere d_{eq}, of case 1, defined in Table I.

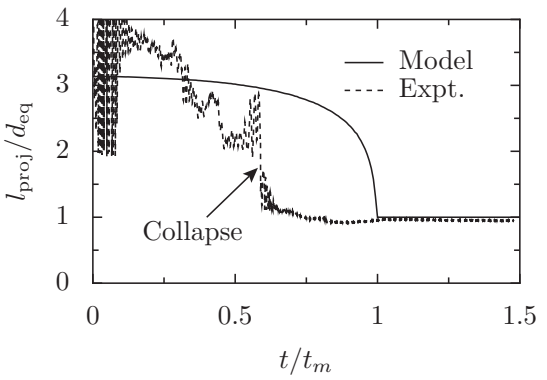

FIG. 8. Projected length of case 2, defined in Table I.

A nearly spherical particle with an aspect ratio of $E = 1.1$ is considered in case 3. In this case, the melting in stage IV dominates the process. This stage corresponds to the one-dimensional sphere model. If the aspect ratio is further reduced, the duration of stages II and III decrease until at $E = 1$ the sphere model is recovered.

Figure 9 shows the modeled surface area A_A nondimensionalized with the surface of a volume equivalent sphere A_{Sp} as the particle melts. During the first stage this area remains constant as no phase change occurs. The second stage exhibits a nearly linear surface area change and makes up most of the melting time in all of the considered cases, except the spherical particle shown in Fig. 4. The theory predicts the end of the second stage at the time instant $t \approx 0.8t_m$, which agrees very well with the experimental observations for a wide range of parameters. It is obvious that a model based on a spherical particle shape is not able to predict such times, typical for the nonspherical shapes.

Figure 10 shows the predictions made by the spheroid model for the total melting times in comparison with experimental data. In the experiments the initial ice crystal temperature was between −18 and −17 °C, the air velocity ranged between 0.75 and 1.25 m/s, the relative humidity between 2.2 and 78%, and the characteristic particle size varied between 0.5 and 1.2 mm. While for the model always a prolate

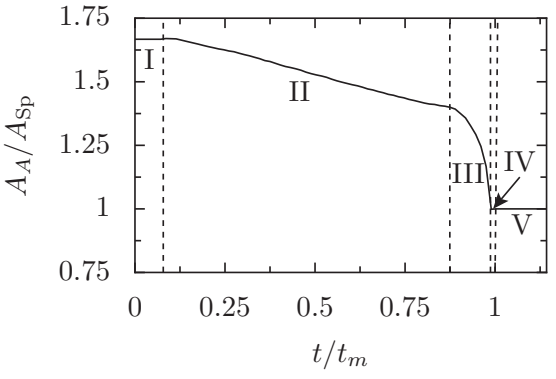

FIG. 9. Ratio of the modeled surface area A_A to the surface area of a volume equivalent sphere A_{Sp} during the melting process. The distinct melting stages are indicated by dashed vertical lines. The operational parameters are the same as in Fig. 3 (case 2 from table I).

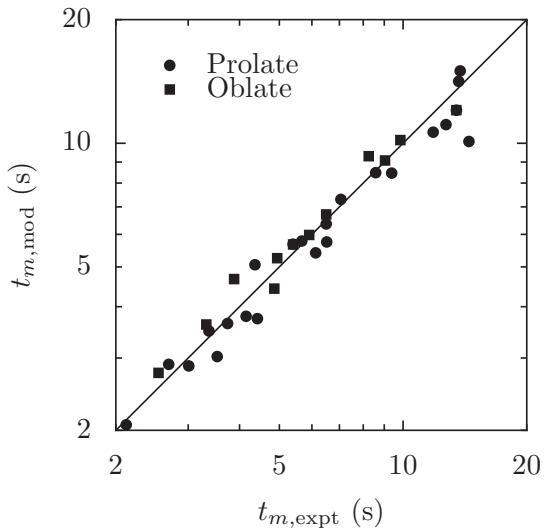

FIG. 10. Comparison of the theoretical predictions (spheroid model) for the total particle melting time with the experimental data. The data include also the total melting times of the particles collapsed during the melting process.

shape was assumed, the real particles exhibited prolate and oblate geometries, indicated by the symbol.

Comparing the results obtained by the presented model and with the one-dimensional sphere model, the difference in melting time only depends on the aspect ratio and the initial temperature T_0 of the particle. Figure 11 shows the melting time difference between the models Δt normalized with the melting time of the spheroid $t_{m,E}$ over the aspect ratio. At $E = 1$, the models coincide and no difference emerges. With increasing aspect ratio, the difference between the models increases. A melting process with no warming up of the particle, i.e., $T_0 = 0\,^{\circ}\mathrm{C}$ is shown as a solid line, while the dashed lines correspond to particle starting temperatures of $T_0 = -20$, -40, and $-60\,^{\circ}\mathrm{C}$. The colder the particle initially is, the larger this difference becomes.

The temporal development of the melt volumetric ratio predicted by the sphere model is linear due to the constant

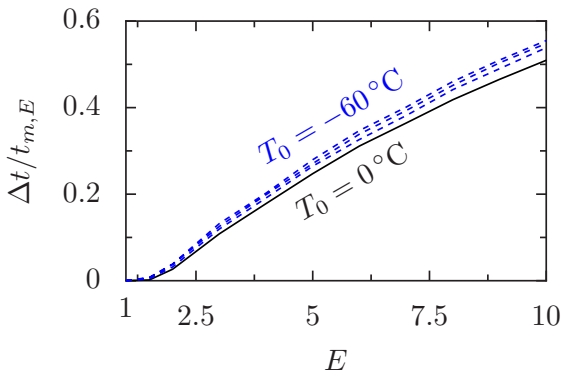

FIG. 11. (Color online) Difference of melting time predicted by the sphere model and the spheroidally assumed particle over the aspect ratio E.

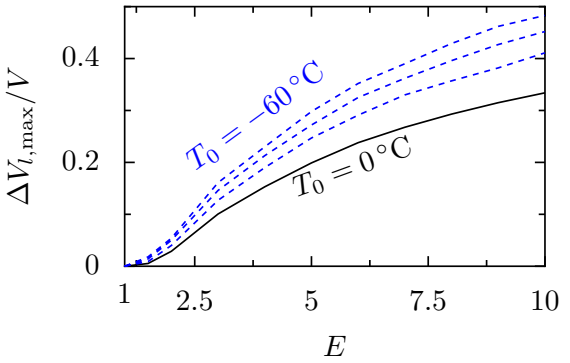

FIG. 12. (Color online) Maximum deviation of the particle's water content during melting between the sphere model and the model in the present study.

surface area over the entire melting process. In this study the surface area is time dependent, resulting in a nonconstant heat flux and, therefore, a nonlinear development of the melt ratio in time. This leads to a time dependent deviation in the melt ratio between the two models, which is zero at the beginning and at the end of the melting process and has a maximum in-between. This maximum deviation of water volume $\Delta V_{l,\mathrm{max}}$ normalized with the entire particle volume V, yielding the melt ratio, is shown in Fig. 12. The deviation is shown for four different initial particle temperatures from $0\,^{\circ}\mathrm{C}$ to $-60\,^{\circ}\mathrm{C}$ in steps of $20\,^{\circ}\mathrm{C}$. It rises with increasing aspect ratio E and decreasing particle starting temperature T_0. This result demonstrates the importance of accounting for the particle shape in the modeling of its melting, since the approximation of its shape by a sphere is not appropriate.

V. CONCLUSIONS

An experimental investigation of the melting process of nonspherical particles is carried out using an acoustic levitator. Phenomena, typical for process, are observed and explained. It is shown that for melting of ice particles the simplified approach, which neglects the heat conduction in the solid and liquid parts in comparison to the latent heat, is valid.

A simple method is proposed which is able to describe the shape change during melting of a nonspherical particle. Using this model, the main phenomena associated with nonspherical particle melting (collection of the liquid in the midregion of the particle, appearance of sharp cusps, smoothing of the particle roughness) are reproduced and explained. Theoretically predicted melting times agree well with the experimental data. Moreover, the differences in the obtained results in terms of melting times and water content of the particle are discussed.

ACKNOWLEDGMENTS

This project has received funding from the European Union's Seventh Framework Programme for research, technological development, and demonstration under Grant Agreement No. ACP2-GA-2012-314314.

[1] H. S. Carslaw and J. C. Jaeger, *Conduction of Heat in Solids* (Oxford University Press, Oxford, UK, 1959).
[2] R. I. Pedroso and G. A. Domoto, J. Heat Transfer **95**, 42 (1973).
[3] D. S. Riley, F. T. Smith, and G. Poots, Int. J. Heat Mass Transfer **17**, 1507 (1974).
[4] S. Tabakova, F. Feuillebois, and S. Radev, Proc. R. Soc. London, Ser. A **466**, 1117 (2010).
[5] K. Stewartson and R. Waechter, Proc. R. Soc. London, Ser. A **348**, 415 (1976).
[6] A. M. Soward, Proc. R. Soc. London, Ser. A **373**, 131 (1980).
[7] S. W. McCue, B. Wu, and J. M. Hill, Proc. R. Soc. London, Ser. A **464**, 2055 (2008).
[8] G. B. Davis and J. M. Hill, IMA J. Appl. Math. **29**, 99 (1982).
[9] J. M. Hill and A. Kucera, Chem. Eng. Sci. **38**, 1360 (1983).
[10] M. A. Herrero and J. J. L. Velázquez, SIAM J. Math. Anal. **28**, 1 (1997).
[11] S. W. McCue, J. R. King, and D. S. Riley, J. Eng. Math. **52**, 389 (2005).
[12] A. L. London and R. A. Seban, Trans. ASME **65**, 771 (1943).
[13] F. Kreith and F. E. Romie, Proc. R. Soc. London, Ser. B **68**, 277 (1955).
[14] B. J. Mason, Q. J. R. Meteorol. Soc. **82**, 209 (1956).
[15] J. Wang, M. Yang, and Y. Zhang, Int. J. Heat. Mass Transfer **80**, 309 (2015).
[16] C. Konrad, Y. Zhang, and Y. Shi, Int. J. Heat. Mass Transfer **50**, 2236 (2007).
[17] C. Tseng and R. Viskanta, Int. J. Heat. Mass Transfer **49**, 2995 (2006).
[18] S. Gu and S. Kamnis, Surf. Coat. Technol. **203**, 3485 (2009).
[19] A. Richter and P. A. Nikrityuk, Powder Technol. **249**, 463 (2013).
[20] H. Gan, J. J. Feng, and H. H. Hu, Int. J. Multiphase Flow **29**, 751 (2003).
[21] R. S. Berry, J. Jellinek, and G. Natanson, Phys. Rev. A **30**, 919 (1984).
[22] E. Molz, A. P. Y. Wong, M. H. W. Chan, and J. R. Beamish, Phys. Rev. B **48**, 5741 (1993).
[23] J. C. Melrose, AIChE J. **12**, 986 (1966).
[24] A. E. Larsen and D. G. Grier, Phys. Rev. Lett. **76**, 3862 (1996).
[25] F. Pacheco-Vázquez, G. A. Caballero-Robledo, and J. C. Ruiz-Suárez, Phys. Rev. Lett. **102**, 170601 (2009).
[26] B. Turnbull, Phys. Rev. Lett. **107**, 258001 (2011).
[27] J. S. Olafsen and J. S. Urbach, Phys. Rev. Lett. **95**, 098002 (2005).
[28] N. Fukuta, R. C. Savage, G. J. Donovan, and C. M. Liu, Technical Report No. AFGL-TR-83-0066, University of Utah, 1982.
[29] S. Mitra, O. Vohl, M. Ahr, and H. Pruppacher, J. Atmos. Sci. **47**, 584 (1990).
[30] R. Oraltay and J. Hallett, Atmos. Res. **24**, 169 (1989).
[31] L. Pawlowski, *The Science and Engineering of Thermal Spray Coatings* (Wiley, Chichester, 2008).
[32] J. He, M. Ice, and E. Lavernia, J. Therm. Spray Technol. **10**, 83 (2001).
[33] Y. Dutil, D. R. Rousse, N. B. Salah, S. Lassue, and L. Zalewski, Renewable Sustainable Energy Rev. **15**, 112 (2011).
[34] M.-Y. Zhou and P. Sheng, Phys. Rev. B **43**, 3460 (1991).
[35] Y. Q. Wang, W. S. Liang, and C. Y. Geng, J. Nanopart. Res. **12**, 655 (2010).
[36] P. Pawlow, Z. Phys. Chem. **65**, 545 (1909).
[37] H. Watanabe, S. Yukawa, and N. Ito, Phys. Rev. E **71**, 016702 (2005).
[38] H. Attar, M. Bönisch, M. Calin, L.-C. Zhang, S. Scudino, and J. Eckert, Acta Mater. **76**, 13 (2014).
[39] J.-P. Kruth, L. Froyen, J. Van Vaerenbergh, P. Mercelis, M. Rombouts, and B. Lauwers, J. Mater. Process. Technol. **149**, 616 (2004).
[40] J. M. Williams, A. Adewunmi, R. M. Schek, C. L. Flanagan, P. H. Krebsbach, S. E. Feinberg, S. J. Hollister, and S. Das, Biomaterials **26**, 4817 (2005).
[41] J. G. Mason, P. Chow, and D. M. Fuleki, J. Eng. Gas Turb. Power **133**, 041201 (2011).
[42] Y. Furukawa and J. S. Wettlaufer, Phys. Today **60** (12), 70 (2007).
[43] A. J. Heymsfield, A. Bansemer, P. R. Field, S. L. Durden, J. L. Stith, J. E. Dye, W. Hall, and C. A. Grainger, J. Atmos. Sci. **59**, 3457 (2002).
[44] R. Rasmussen and H. Pruppacher, J. Atmos. Sci. **39**, 152 (1982).
[45] R. Rasmussen, V. Levizzani, and H. Pruppacher, J. Atmos. Sci. **41**, 374 (1984).
[46] R. Rasmussen, V. Levizzani, and H. Pruppacher, J. Atmos. Sci. **41**, 381 (1984).
[47] A. L. Yarin, G. Brenn, J. Keller, M. Pfaffenlehner, E. Ryssel, and C. Tropea, Phys. Fluids **9**, 3300 (1997).
[48] A. L. Yarin, M. Pfaffenlehner, and C. Tropea, J. Fluid Mech. **356**, 65 (1998).
[49] See Supplemental Material at http://link.aps.org/supplemental/10.1103/PhysRevE.92.033012 for links to the videos, corresponding to Figs. 2–4.
[50] C. A. Knight, J. Atmos. Sci. **36**, 1123 (1979).
[51] K. Gunn and J. Marshall, J. Meteor. **15**, 452 (1958).
[52] C. A. Knight, J. Colloid Interface Sci. **25**, 280 (1967).
[53] J. M. Back, S. W. McCue, and T. J. Moroney, Sci. Rep. **4**, 7066 (2014).
[54] G. B. Whitham, *Linear and Nonlinear Waves* (Wiley, New York, 1999).
[55] J. A. Sethian, *Level Set Methods and Fast Marching Methods* (Cambridge University Press, Cambridge, 1999).
[56] I. H. Bailey and W. C. Macklin, Q. J. R. Meteorol. Soc. **94**, 1 (1968).
[57] A. L. Yarin and D. A. Weiss, J. Fluid Mech. **283**, 141 (1995).
[58] I. V. Roisman and C. Tropea, J. Fluid Mech. **472**, 373 (2002).
[59] S. Howison, J. Ockendon, and A. Lacey, Q. J. Mech. Appl. Math. **38**, 343 (1985).
[60] VDI-Gesellschaft Verfahrenstechnik und Chemieingenierwesen (GVC), ed., *VDI-Wärmeatlas: Berechnungsblätter für den Wärmeübergang (German Edition)*, 10th ed. (Springer, Vieweg, 2005).
[61] F. M. Orr, L. E. Scriven, and A. P. Rivas, J. Fluid Mech. **67**, 723 (1975).